

Open cluster age calibration from colour-magnitude morphological indices using *Gaia* DR3 data

F. A. Ferreira^{1*}, J. F. C. Santos Jr.¹, W. J. B. Corradi^{1,4}, M. S. Angelo³,
and F. F. S. Maia²

¹Universidade Federal de Minas Gerais, Departamento de Física, Av. Antônio Carlos 6627, 31270-901, Brazil

²Universidade Federal do Rio de Janeiro, Instituto de Física, 21941-972, Brazil

³Centro Federal de Educação Tecnológica de Minas Gerais, Av. Monsenhor Luiz de Gonzaga, 103, 37250-000, Brazil

⁴Laboratório Nacional de Astrofísica, R. Estados Unidos, 154, 37504-364, Itajubá, MG, Brazil

Accepted XXX. Received YYY; in original form ZZZ

ABSTRACT

Star clusters are crucial for understanding how stars evolve. Their colour-magnitude diagrams show the effects of stellar evolution of approximately coeval objects with the same chemical composition. Furthermore, the determination of their astrophysical parameters (age, distance, colour excess and metallicity) together with their spatial distribution provides information about the structure and the evolution of the Galaxy itself. Using data from the *Gaia* DR3 and 2MASS catalogues, we develop methodologies for characterizing open clusters. Precise membership lists, mean astrometric parameters and radii are obtained. Using photometric data from both data sources, we carried out new age calibrations that rely on morphological indices based on colour (ΔBR) and magnitude (ΔG) differences between the red clump and the turnoff for a sample of 34 open clusters with ages covering the interval $8.3 < \log[t(\text{yr})] < 9.9$. A set of age calibration functions based on *Gaia* morphological age indices are determined for the first time. We demonstrate their accuracy, obtaining a mean residual of 0.06 dex in $\log[t(\text{yr})]$. Our results also show that stellar evolution models tend to predict the difference ΔG . However, they typically overestimate the difference ΔBR for objects younger than $\log[t(\text{yr})] = 8.8$.

Key words: Galaxy: stellar content – open clusters and associations: general – surveys: *Gaia*

1 INTRODUCTION

Open clusters (OCs) are important objects to study the history and structure of the Galactic disc. Young OCs reveal how stars form in embedded environments as well as the recent disc history (Lada & Lada 2003). On the other hand, the older OCs are the fingerprints of the chemical and dynamical evolution of the Galactic disc (e.g. Friel 1995; Carraro et al. 2007; Netopil et al. 2016 [hereafter N2016]; Cantat-Gaudin et al. 2020 [hereafter C2020]).

The Galactic OCs present a vast range of ages ($\log[t(\text{yr})] \lesssim 10.0$) and typically solar metallicities ($-0.5 \lesssim [Fe/H] \lesssim 0.5$) (Kharchenko et al. 2013; N2016; Dias et al. 2021 [hereafter D2021]). Their colour-magnitude diagrams (CMDs) contain the fiducial positions of evolving stars of different masses according to their evolutionary stages at a given age, allowing us to study in detail the stellar evolution.

The separation between fiducial OCs members from field stars, especially in high stellar density environments, like the Galactic disc, is a challenging task. However, due to the high precision of the astrometric and photometric data provided by the most recent releases of the *Gaia* catalogue (DR2: Lindegren et al. 2018; Evans et al. 2018; EDR3: *Gaia* Collaboration et al. 2021, DR3: *Gaia* Collaboration et al. 2023) it has been possible to disentangle both cluster and field populations, allowing a drastic increase of works providing precise memberlists of OCs (Cantat-Gaudin et al. 2018; Angelo et al. 2019, 2021; D2021). Combined with efficient methodologies, a number of new objects has been discovered (Ferreira et al. 2019; Sim et al. 2019; Ferreira et al. 2020; Castro-Ginard et al. 2020; Ferreira et al. 2021; He et al. 2022; Hunt & Reffert 2023 [hereafter H2023]).

By taking advantage of the resulting decontaminated CMDs from such precise member star lists, the stellar populations from OCs can be better studied. An important feature, known as the Red Clump (RC), characteristic of intermediate age and older stellar populations whose more

* E-mail: filipe1906@ufmg.br

massive stars are passing through the evolutionary stage of Helium burning in the core, can be easily noticed (see Figs 2, 3 and 10 from [Gaia Collaboration et al. 2018](#)). The RC is a concentration of cold and luminous stars which occurs after the Red Giant Branch (RGB) phase in the CMD, and is the longest subsequent evolutionary stage in the life of a star, after the Main Sequence (MS). The RC is not often observed in the CMD of very young clusters, because the He-burning phase is rapid in the more massive stars, thereby it has been reported for clusters within the age interval of $8.3 \lesssim \log[t(\text{yr})] \lesssim 10.0$ ([Grocholski & Sarajedini 2002](#); [van Helshoecht & Groenewegen 2007](#); [Onozato et al. 2019](#)).

The RC is widely used as a standard candle, because although the colours of stars in this evolutionary phase depend strongly on age and metallicity, for low-mass stars ($M \lesssim 1.9M_{\odot}$) the absolute magnitude do not show large variations, especially in the infrared. In this way, by establishing a reliable RC mean magnitude value for old populations ($\log[t(\text{yr})] \gtrsim 9.0$), we are capable to determine distances to structures within our Galaxy and to neighboring galaxies ([Grocholski & Sarajedini 2002](#); [van Helshoecht & Groenewegen 2007](#); [Bilir et al. 2013](#); [Girardi 2016](#); [Onozato et al. 2019](#)).

For intermediate age and older clusters $8.3 \lesssim \log[t(\text{yr})] \lesssim 10.0$, the average position of the RC stars in the CMD can also be used as an age indicator. Indices based on CMD morphology are common in the literature. For example, the difference in magnitude ΔV between the MS turnoff (bluest point on the MS) and the mean magnitude of the RC tend to increase with age for star populations older than 1 Gyr. On the other hand the difference in colour $\Delta(B - V)$ of the same regions tend to decrease with age ([Anthony-Twarog & Twarog 1985](#)). A morphological age index called MAR is also defined by [Anthony-Twarog & Twarog \(1985\)](#), taking the ratio $\Delta V / \Delta(B - V)$.

[Phelps et al. \(1994\)](#) defined the morphological age indices δV and $\delta 1$. The index δV is the difference between the inflection point of the main sequence or the base of the giant branch and the mean magnitude value of the RC, while $\delta 1$ is the colour difference between the point one magnitude brighter than the turnoff and the base of the giant branch. The index δV established in [Phelps et al. \(1994\)](#) was later calibrated with the ages and metallicities of star clusters in [Salaris et al. \(2004\)](#).

Such indices based on the CMD morphology are common in the literature and are well-known age indicators for Galactic clusters ([Anthony-Twarog & Twarog 1985](#); [Phelps et al. 1994](#); [Salaris et al. 2004](#); [Piatti et al. 2010](#); [Beletsky et al. 2009](#); [Oralhan et al. 2015](#)) and Magellanic Clouds clusters ([Geisler et al. 1997](#); [Parisi et al. 2014](#)). Those age determination techniques are independent of distance and reddening, but it is necessary the consistent identification of those key evolutionary features in the CMDs.

In this work, we used data from the 2MASS ([Skrutskie et al. 2006](#)) and *Gaia* DR3 catalogues to establish morphological age indices for a set of Galactic OCs, extending the morphological age indices for OCs as young as $\log[t(\text{yr})] = 8.3$. We adopted the magnitude difference between the turnoff point and the RC, an index widely employed as an age indicator, both in the visible (ΔV , [Carraro & Chiosi 1994](#)) and in the infrared (ΔK , [Beletsky et al. 2009](#);

[Zasowski et al. 2013](#)). We also present age calibrations with those indices, using the 2MASS index ΔK as a benchmark.

This paper is structured as follows. In Section 2 the data is presented. In Section 3 the OC sample selection is described. In Section 4 the analysis procedures are discussed, including membership assessment and determination of mean astrometric parameters. The CMDs properties of our OC sample are explored in Section 5. The main results are presented in Section 6 and the concluding remarks are given in Section 7.

2 DATA

2.1 *Gaia*

The *Gaia* DR3 catalogue provides positions, proper motions in right ascension and declination, parallaxes and photometry (G , G_{BP} , and G_{RP} passbands) for nearly two billion sources. The Gaia@AIP (<https://gaia.aip.de/>) online services have been used to extract *Gaia* DR3 data for each OC in circular regions centred on the coordinates presented in D2021 catalogue. For a first guess, we adopted an extraction radius of 1, 2 and 3 degrees for OCs of heliocentric distances $d > 2$ kpc, $1 \text{ kpc} < d < 2 \text{ kpc}$ and $d < 1 \text{ kpc}$, respectively. Those sizes were large enough to restrict the studied OCs and an adjacent comparison star field. Confirmed OCs in D2021 present mean tidal radius (r_t) of 9.85 pc with standard deviation of 5.21 pc ([Kharchenko et al. 2013](#)). Assuming a typical superior limit in OC size of $r_t \sim 15$ pc, an OC would appear to have apparent radii of ~ 26 arcmin at 2 kpc, ~ 52 arcmin at 1 kpc and ~ 104 arcmin at 500 pc. This means that those extracting radii are capable to encompass a typical OC at those ranges of distances.

To extract the data with the corrected version of the photometric flux excess factor ([Riello et al. 2021](#)), we adopted the query examples presented in *Gaia* EDR3 documentation (Appendix B, [Gaia Collaboration et al. 2021](#)). We also adopted a filter to keep only stars with $G < 19$ to avoid less informative sources, which is also the nominal magnitude limit to ensure astrometric and photometric completeness ([Lindgren et al. 2021](#)).

In order to correct the original data for the parallax zero-point bias, we applied the available recipe presented in [Lindgren et al. \(2021\)](#), which is applied equally to *Gaia* EDR3 and to *Gaia* DR3 astrometry. This correction is provided separately for sources with available 5- and 6-parameter astrometric solutions and is given as a function of the source magnitude, colour, and celestial position. No further corrections in flux or G-band magnitudes have been applied, since they are already implemented in DR3.

We applied quality filters limiting our database to remove spurious astrometric and photometric solutions by keeping sources consistent with the two following equations:

$$|C^*| < 5\sigma_{C^*} \quad (1)$$

$$RUWE < 1.4, \quad (2)$$

where C^* is the corrected value of the BP and RP flux excess factor, σ_{C^*} is given by equation 18 of [Riello et al. \(2021\)](#)

and RUWE is the renormalised unit weight error (Lindgren et al. 2021).

2.2 2MASS

The Two Micron All Sky Survey (2MASS) provides positions and near-infrared photometry (J , H , and K passbands) for nearly 470 million sources, covering the entire sky. For each target, we have used the VizieR service to extract data from the 2MASS catalogue for stars inside the circular regions quoted above. To ensure quality to our sample, we only extracted stars with 2MASS JHKs photometric quality flag 'AAA'. We then crossmatched *Gaia* catalogue with 2MASS by selecting 2MASS sources within 1 arcsec from *Gaia* sources. The photometric depth of our catalogues is governed by *Gaia* photometry, in other words, if a star from *Gaia* do not have a counterpart in 2MASS survey, this star is not excluded.

3 THE OC SAMPLE

It is beyond the scope of this work to determine the astrophysical parameters of the OCs (age, distance, color excess, and metallicity). Therefore, we decided to use the OC catalogue published by N2016, which contains a homogenized sample of 172 OCs with averaged ages and metallicities, based on $[Fe/H]$ abundances from numerous individual studies, as well as their associated uncertainties. To select our OC sample, we restricted their catalogue to objects closer than 3 kpc from the Sun according to D2021 and for which metallicities were taken from high resolution spectroscopy. For the remaining sample, we kept OCs for which we could visually identify in the CMD a concentration of stars around the RC position and for which the turnoff points are brighter than $G = 19$, resulting in a final sample of 34 OCs, covering $8.3 < \log t[yr] < 9.9$ and $-0.44 < [Fe/H] < 0.37$.

The catalogue presented in N2016 is widely adopted, especially as a reference for metallicity (Bossini et al. 2019; Chen & Zhao 2020; Zhang et al. 2021; Im et al. 2023) and recent works still adopt their age values (Chen & Zhao 2020). To ensure the quality of their data as age references for the range of ages and distances explored in this work, we compared the selected sample of OCs with recent catalogs based on *Gaia* data (C2020; D2021; H2023). The comparison between the age values reported by these catalogs is presented in Table 1. The age values in N2016 do not show significant offsets from recent literature values, and their comparison with recent catalogs exhibits similar correlations and residuals, as observed when catalogs based on *Gaia* photometry are compared with each other. The only discrepant age value found was for the OC NGC2354, whose age value was not included in the comparisons. A discussion concerning this particular OC is presented in Appendix A1.

We have also compiled distances and colour excesses from D2021. Positions, ages, metallicities, distances and colour excesses of our sample are presented in Table 2.

Table 1. Comparison between the adopted age values from N2016 with recent catalogues based on *Gaia* data. The parameter $\Delta \log t$ represents the average difference between the first source and the second source. The mean residuals and the correlation between them are also reported.

Sources	$\Delta \log t$	Mean residuals	Correlation
	<i>dex</i>	<i>dex</i>	
N2016 x C2020	-0.05	0.10	0.95
N2016 x D2021	-0.07	0.09	0.97
N2016 x H2023	0.03	0.17	0.82
H2023 x C2020	-0.07	0.15	0.79
H2023x D2021	-0.1	0.13	0.84
C2020 x D2021	-0.02	0.07	0.97

4 METHODOLOGY

To assess memberships and remove the field population from the clusters sample, we have employed proper motion and parallax selections of members. For this purpose, we have developed a methodology based on Ferreira et al. (2019) that includes:

- (i) Preliminary analysis of Vector Point Diagrams (VPDs) to determine the mode of the cluster's proper motion distribution for both components;
- (ii) Construction of a proper motion mask around the determined proper motion mode, to create a subsample almost free of contamination from field stars;
- (iii) Determination of the cluster centre and radius by building radial density profiles (RDPs);
- (iv) Gaussian fittings over the proper motion components and parallaxes distributions and filters restricting stars based on such distributions.

4.1 The clusters proper motion detection

To find the OCs signatures in the VPD, we used the same method adopted in Ferreira et al. (2019; 2020; 2021), where a colour filter is applied on the sample to discard very reddened field stars and maximize the contrast between cluster and field population. We started with a colour threshold value $G_{BP} - G_{RP} < 2.5$. For the cases of more distant and highly reddened clusters, we increased this threshold value and, for cases of less reddened ones, this value is decreased, in order to make the initial detection of the cluster evident as an overdensity in the VPD. We then computed the mode of the proper motions in right ascension (μ_{α}^*) and declination (μ_{δ}).

In Fig. 1 we show how we identified the proper motion signature for the OC IC 4756. The top left panel shows a VPD for all stars within 2 degrees from its centre, containing 629323 stars, showing that without any filter, we are not capable to find the cluster. In the top right panel, a colour filter is represented by the red line $G_{BP} - G_{RP} < 1.20$, selecting the cyan sample, which corresponds to 8402 stars. In the bottom left panel, the VPD with the sample filtered by colour (yellow and brown samples) is plotted over the entire sample

Table 2. Properties of the investigated clusters from the literature.

OC	α_{J2000} degrees	δ_{J2000} degrees	$\log[t(\text{yr})]$ dex	$\sigma_{\log[t(\text{yr})]}$ dex	$[Fe/H]$ dex	$\sigma_{[Fe/H]}$ dex	d pc	σ_d pc	$E(B - V)$ mag	$\sigma_{E(B - V)}$ mag
NGC 188	11.749	85.243	9.80	0.17	0.11	0.04	1859	36	0.075	0.008
NGC 752	29.120	37.760	9.23	0.18	-0.03	0.06	441	4	0.051	0.024
NGC 1245	48.699	47.253	9.03	0.09	0.02	0.03	2763	97	0.268	0.010
NGC 1817	78.153	16.695	8.91	0.17	-0.11	0.03	1582	40	0.233	0.012
NGC 2099	88.048	32.568	8.56	0.25	0.02	0.05	1299	22	0.297	0.016
Trumpler 5	99.107	9.454	9.64	0.21	-0.44	0.07	3260	122	0.652	0.007
Collinder 110	99.681	2.100	9.09	0.24	0.03	0.02	1991	80	0.530	0.021
NGC 2354	108.520	-25.725	9.14*	0.06 *	-0.18	0.02	1258	42	0.171	0.019
NGC 2355	109.269	13.766	8.91	0.08	-0.05	0.08	1794	41	0.104	0.006
NGC 2360	109.447	-15.623	9.04	0.27	-0.03	0.06	1054	21	0.132	0.020
NGC 2423	114.310	-13.880	8.90	0.19	0.08	0.05	924	14	0.095	0.021
NGC 2420	114.603	21.576	9.37	0.13	-0.05	0.02	2435	46	0.038	0.005
NGC 2447	116.150	-23.872	8.60	0.17	-0.05	0.01	1004	10	0.037	0.012
NGC 2477	118.054	-38.505	8.93	0.1	0.07	0.03	1351	47	0.384	0.025
NGC 2527	121.280	-28.150	8.81	0.12	-0.10	0.04	630	8	0.075	0.018
NGC 2539	122.665	-12.830	8.70	0.11	-0.02	0.08	1243	50	0.069	0.002
NGC 2660	130.665	-47.203	9.12	0.09	0.04	0.03	2642	105	0.470	0.048
NGC 2682	132.822	11.839	9.54	0.15	0.03	0.05	865	18	0.041	0.013
IC 2714	169.370	-62.710	8.45	0.14	0.02	0.06	1229	16	0.393	0.013
NGC 3960	177.650	-55.684	8.99	0.10	-0.04	0.10	2074	114	0.347	0.027
NGC 4337	186.022	-58.121	9.24	0.11	0.12	0.05	2416	99	0.418	0.021
NGC 4349	186.070	-61.875	8.52	0.27	-0.07	0.06	1656	36	0.420	0.019
Collinder 261	189.56	-68.400	9.86	0.17	0.00	0.04	2806	119	0.322	0.035
NGC 5822	225.900	-54.300	8.95	0.11	0.08	0.08	796	27	0.155	0.019
NGC 6134	246.950	-49.150	8.96	0.16	0.11	0.07	1055	51	0.411	0.024
NGC 6253	254.770	-52.715	9.59	0.13	0.34	0.11	1674	72	0.256	0.019
IC 4651	261.179	-49.917	9.27	0.18	0.12	0.04	920	15	0.113	0.017
NGC 6583	273.960	-22.150	9.00	0.10	0.37	0.04	2162	132	0.592	0.041
IC 4756	279.670	5.520	8.82	0.08	0.02	0.04	472	1	0.204	0.012
NGC 6705	282.790	-6.255	8.28	0.19	0.12	0.09	1888	65	0.470	0.016
Ruprecht 147	289.100	-16.350	9.37	0.04	0.16	0.08	305	0	0.094	0.016
NGC 6811	294.350	46.390	8.86	0.11	0.03	0.01	1102	13	0.069	0.011
NGC 6819	295.332	40.192	9.32	0.09	0.09	0.01	2444	54	0.157	0.016
NGC 7789	359.330	56.720	9.18	0.06	0.05	0.07	1907	30	0.328	0.008

* Age calculated based on recent literature parameters (see Sect A1).

(gray dots), exhibiting an overdensity of stars corresponding to the cluster, where the red lines mark its proper motion modes at $\mu_\alpha^* = 1.28 \text{ mas yr}^{-1}$ and $\mu_\delta = -4.98 \text{ mas yr}^{-1}$. The same VPD with the colour filtered sample, including histograms where the proper motion modes are indicated, is shown in the bottom right panel.

4.2 The proper motion filter

In order to estimate how the dispersion in proper motion components of real OCs behave (on average) as function of distance, we used the recent catalogue published by H2023, where the OCs members were obtained by using HDBSCAN algorithm over *Gaia* DR3 data. We built a sample by limiting the OCs to distances between 40 pc and 6 kpc and number of members larger than 200. The catalogue used provides, for each OC, its position, astrophysical parameters, and the mean astrometric parameters and dispersions presented by its probable members. We then separated the OCs into intervals of 50 pc and calculated the mean proper motion dispersion values for the entire group of OCs within each distance interval. In this procedure, we established a

small catalog of distances and the expected OC proper motion dispersions at those distances.

As shown in Fig. 2, we note that the nearest clusters tend to exhibit higher dispersion values, due to the apparent random motion of the stars being greater than the proper motion uncertainties. On the other hand, clusters located at distances farther than 2 kpc tend (on average) to exhibit an approximately fixed value, which shows that beyond this limit the physical dispersion of proper motions tends to be negligible in face of astrometric errors. In this way, we adopted an exponential fitting over these data to reproduce this behavior for both proper motion components (Fig. 2).

This procedure was carried out to construct proper motion masks of sizes that fit the clusters proper motion spread for different distances. From the mean values σ_{rep} of proper motion dispersion, we adopted boxes with sides equal to 20 times this value, that is, we limited the samples of stars within $10 \sigma_{rep}$ around the mode of the proper motion distributions for both components (Fig 3). The adopted sizes of the proper motion masks were:

$$L_{pmra} = 20 \times [0.895 \times \exp(-0.0027 \times D_{cluster}) + 0.094] \quad (3)$$

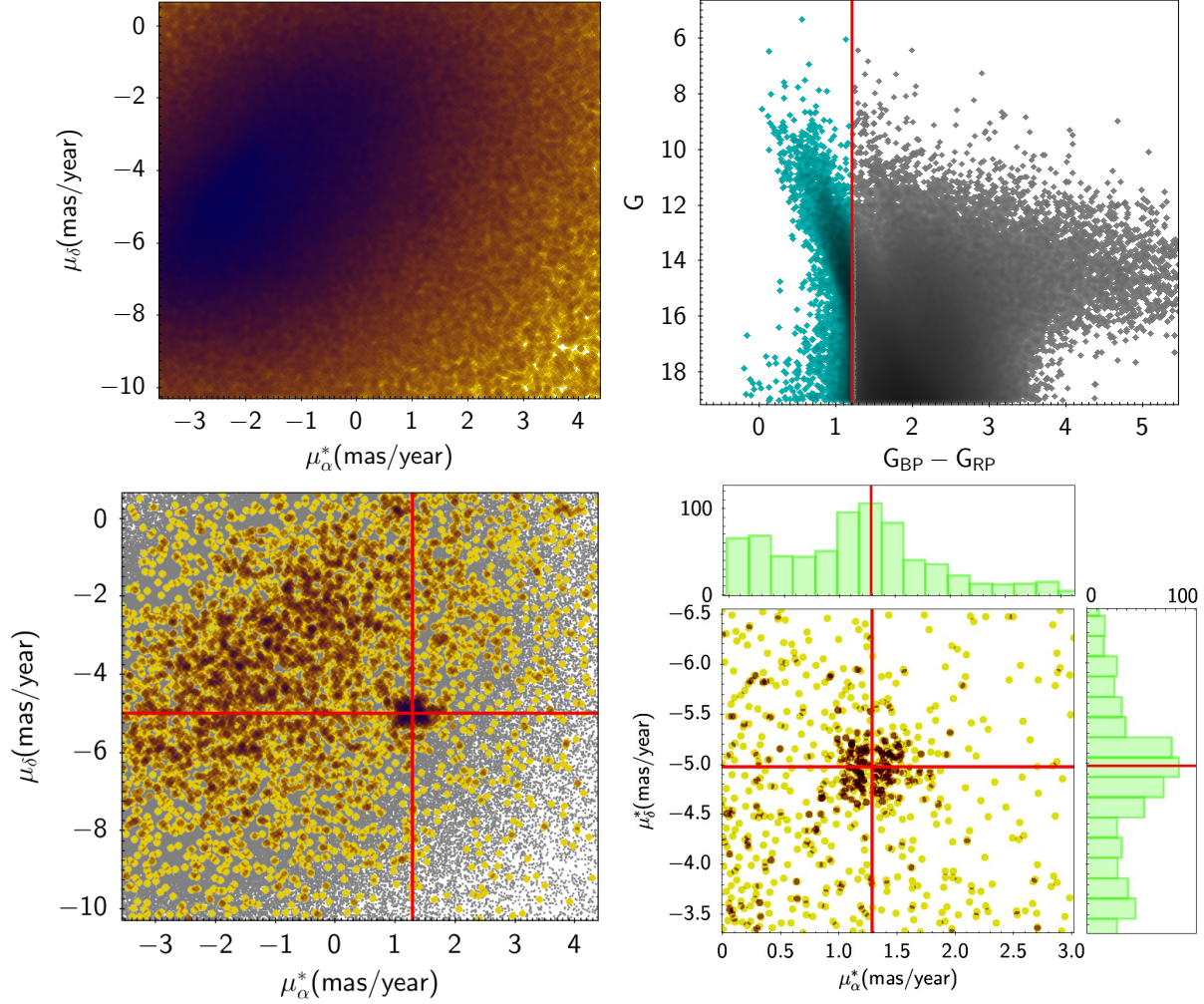


Figure 1. Data inspection for the OC IC 4756. Top left: VPD of all data within 2 degrees radii from its centre, containing 629323 stars. Top right: CMD built from the entire sample (grey dots), where the colour filter is represented by the red line, selecting the cyan sample, which corresponds to 8402 stars. Bottom left: VPD with the sample filtered by colour (yellow and brown samples) plotted over the entire sample (grey dots), the red lines mark the proper motion peak. Bottom right: The same VPD with the colour filtered sample, but with the histograms represented where the proper motion peak values were determined.

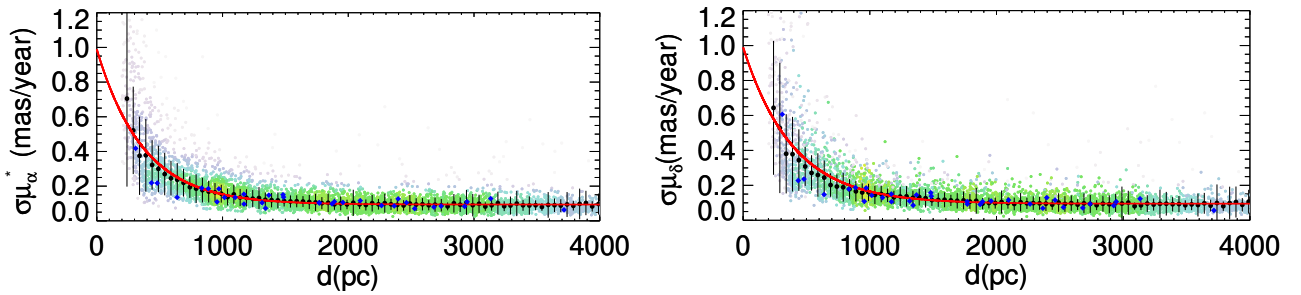


Figure 2. Mean values of dispersion in μ_{α}^* (top) and μ_{δ} (bottom) for a set of 1229 OCs as function of the heliocentric distance. The red lines represent the best exponential fit, the coloured symbols represent the density of OCs and the black filled circles represent the local mean value of proper motion dispersion. Error bars represent the standard deviation in each bin and the blue filled dots represent our sample of OCs.

$$L_{pmde} = 20 \times [0.810 \times \exp(-0.0025 \times D_{cluster}) + 0.095] \quad (4)$$

where $D_{cluster}$ is the distance (in pc) according to D2021 and L_{pmra} and L_{pmde} represent the sizes of the mask in proper motion units in right ascension and declination, respectively. For subsequent analyses, we will abandon any colour filters, as they obviously exclude very cool low main sequence stars from nearby clusters and possible RGB stars for some older clusters. This procedure defines our database. We restricted the OCs proper motion space by employing the box-shaped filter centered on the modal values of μ_{α}^* and μ_{δ} , as shown in the top panels of Fig. 3.

4.3 Centre and radial density profile

After establishing the size of the proper motion mask for our OCs sample, we applied it to the original database to reduce the contamination by field stars. We constructed frequency histograms with the equatorial coordinates of the stars and estimated the centre values of the clusters in both coordinates through Gaussian fittings (taking the average values of the fit). This average value is used as a first guess for the central coordinates to build the RDPs, however the final values are based on the best RDP constructed.

We built the RDPs by counting stars within concentric rings with same thickness as function of the distance to the cluster centre. We repeated this procedure for 4 ring thicknesses (75, 100, 125 and 150 arcseconds, except for the closest clusters, for which larger bin sizes were used) in order to mitigate binning effects on the density distribution. We also computed the density values of the background far from the centre of the cluster. Then, we determined the value of the cluster's limiting radius (r_{lim}) as the distance at which the density level reaches the mean value computed for the sky background (bottom panels, Fig. 3).

In this procedure, we applied small variations in the coordinates of the centre so that the density profile had a well-defined central maximum. The radius containing 50% of the members (r_{50}) was also determined. The OCs Ruprecht 147, NGC 752, IC 4756, NGC 2527 and IC 4651 have their spatial distributions significantly affected by field stars due their projection towards dense star fields and/or due to the fact that they are poor stellar concentrations. Therefore, to build the RDPs for those objects, we adopted a subsample with parallaxes above 0.9 mas to increase the contrast with the field population. Taking into account the expected dispersion in parallax, this selection did not remove members from the respective OCs.

4.4 Two-dimensional proper motion filter and parallax filter

In order to obtain precise member star lists, we established a filter capable of better predicting the morphology of the distribution of stars in the VPD, since the box-shaped masks determined previously tend to encompass regions substantially larger than the dispersions expected for the clusters.

For this purpose, we constructed a two-dimensional histogram of the VPD with the samples restricted by the limiting radius determined for the cluster. Then we also constructed two-dimensional histograms for an adjacent concen-

Table 3. Mean differences ($\Delta\mu_{\alpha}^*$, $\Delta\mu_{\delta}$ and $\Delta\varpi$) between our OCs astrometric parameters (μ_{α}^* , μ_{δ} and ϖ) and 8 coincidental OCs from the literature. The standard deviation is also calculated.

Source	$\Delta\mu_{\alpha}^*$	$\Delta\mu_{\delta}$	$\Delta\varpi$
	mas/year	mas/year	mas
H2023	0.005 ± 0.032	-0.005 ± 0.014	-0.003 ± 0.006
Alf2024	0.005 ± 0.022	0.007 ± 0.010	0.004 ± 0.006

tric annular stellar field with the same area as the cluster: the internal radius of the control field is 1.3 times greater than the limiting radius. In order to remove the contribution of field stars in the proper motion space, we subtracted the histograms and performed 2D Gaussian fittings over the resulting ones. Subsequently, those stars with proper motion components outside $3\text{-}\sigma$ of the 2D Gaussian mean values, considered as proper motion outliers, were removed from the sample.

To discard remaining probable field stars with discrepant parallaxes from the average OC parallax, we performed an one-dimensional Gaussian fitting to the parallax distribution of the sample filtered by proper motion, limiting them to $3\text{-}\sigma$ of the average value (Fig. 4).

4.5 Memberlists

Our OCs memberlists were obtained through the filters mentioned above. The panels in Fig. 4 show the members proper motions and parallaxes distributions and the cleaned CMD. We compared our OCs memberlists with those of recent works (H2023; Alfonso et al. 2024 [hereafter Alf2024]) that used *Gaia* DR3 data to perform membership determination using similar techniques (HDBSCAN). Alf2024 provides memberlists for OCs within 1 kpc. We compared our OCs with those present in both catalogues, resulting in 8 OCs that span a considerable range of sizes and numbers of members. The Table 3 exhibits a comparison between the mean astrometric parameters derived in the studies for coincidental OCs. The mean astrometric parameters derived in this work are in good agreement with the literature, with no significant offsets in the compared values. We also compared the number of member stars in our study ($N_{members}$) with those reported in the literature, as shown in Fig. 5. Our number of members differs from that given by Alf2024, which did not apply a spatial restriction to their OCs, resulting in clusters that appear to encompass more members. In contrast, H2023 reported the total number of members within the tidal radius, which is in good agreement with our results (see Fig. 5).

The Galactic coordinates l and b , r_{lim} , r_{50} , proper motions in right ascension and declination (μ_{α}^* and μ_{δ}), parallaxes (ϖ) and their dispersions and the number of probable members N are presented in Table 4. Tables containing memberlists and all parameters determined for our sample of OCs are available electronically through Vizier¹.

¹ <http://cdsarc.u-strasbg.fr/vizier/cat/J/MNRAS/vol/page>

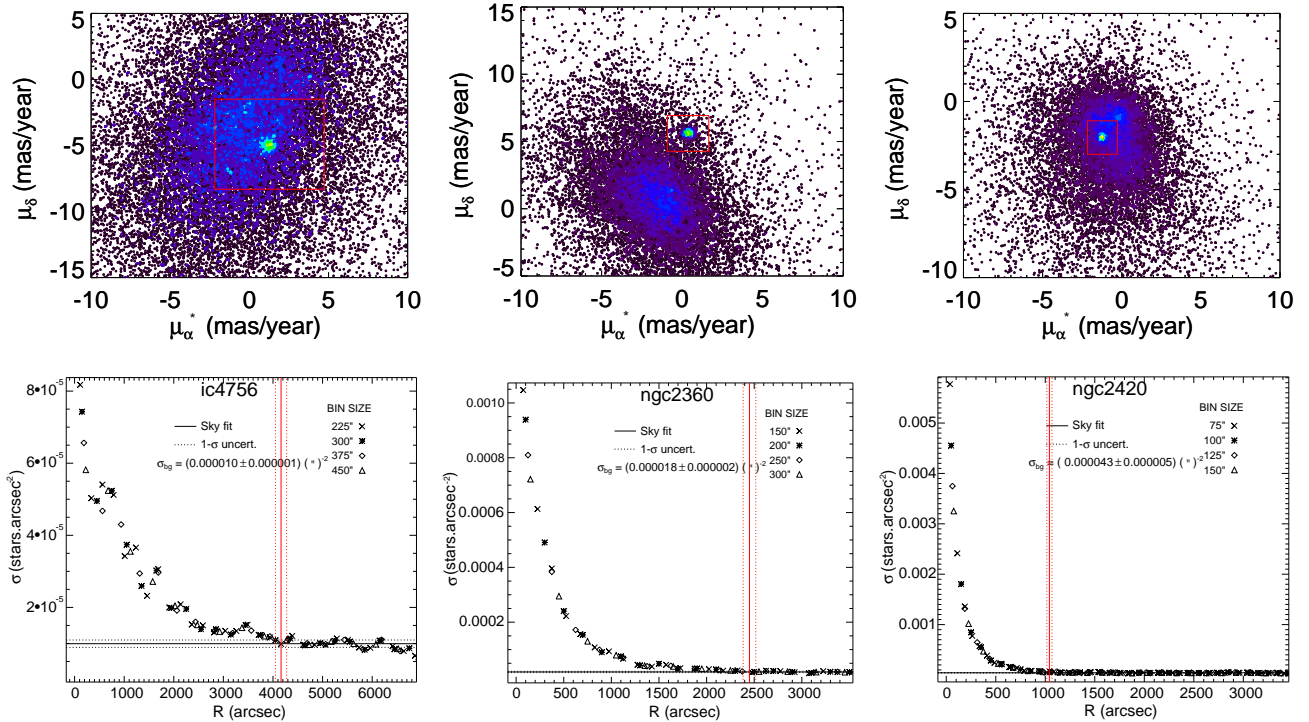


Figure 3. Top: Proper motion mask applied to the VPD for OCs of different distances: IC4756 (left), NGC 2360 (middle) and NGC 2420 (right). Bottom: Radial density profiles of the same OCs: IC4756 (left), NGC2360 (middle), NGC2420 (right) with their limiting radius (vertical red line) and mean background density level (horizontal black line) indicated.

5 RC AND TURNOFF POSITIONS

The position of the RC in the CMD is often obtained by applying a simple filter over the stars distribution to take its mean value in magnitude and/or colour (Grocholski & Sarajedini 2002; Beletsky et al. 2009; van Helshoecht & Groenewegen 2007; Onozato et al. 2019). We determined the mean values and dispersion of colour ($G_{BP} - G_{RP}$ and $J - K$) and magnitudes (G and K) of the RC by restricting the sample in a box with width of 1 mag for G , 0.4 mag for $G_{BP} - G_{RP}$, 1.4 mag for K and 0.4 mag for $J - K$. Those sizes were chosen due to the visual dispersion of the stars in the RC of both visible and infrared CMDs, encompassing the region defined by RC stars. As uncertainties in the colour and magnitude of the RC were adopted the corresponding standard deviation from the mean.

We considered the bluest point of the MS as the turnoff position. However, some OCs of our sample present blue straggler stars and/or remaining field stars in the final memberlist that have colour indices bluer than the expected turnoff position. In order to remove those isolated stars, we identified the number of nearest neighbours of each star from the CMD within squared boxes of width 0.05 mag. We then removed stars with few close neighbours and, from the remaining sample, measured the colour and magnitude values of the bluest star left in the MS.

For CMDs with *Gaia* filters, the removal of stars with only one close neighbour worked for most of our sample, and for only four OCs we had to remove stars with more than three close neighbours. On the other hand, the 2MASS photometry presents larger errors and the removal of stars

with one, two or three close neighbours worked for most of our sample, although in some cases we had to elevate this cutoff value (for five OCs we had to remove stars with more than 6 neighbours). To provide uncertainties, we adopted the standard deviation value of colour and magnitude of the 5 bluest remaining MS stars. For 2MASS data, we did not determine the turnoff position for the OCs NGC 6819, Trumpler 5 and Collinder 261 due the observational limit, which is brighter than the turnoff of such distant and old objects. The scheme used to identify the turnoff positions and RC average magnitudes is summarized in Fig 6.

We also applied a similar procedure for these same evolutionary regions to the PARSEC isochrones (Bressan et al. 2012), with ages and metallicities representative of our OC sample. Initially, we selected stars where the isochrone table label identifier was equal to 1 (MS) and 4, 5 and 6 (He-burning stars = RC). The turnoff position was taken as the bluest point of the MS, however we rejected the blue hook-like structure, that represents stars at the end of the main sequence, in order to keep consistency with the age range analysed.

The RC positions according to the PARSEC isochrones correspond to the point of maximum effective temperature (similar to those displayed in Figure 8 of Ruiz-Dern et al. 2018). Fig. 7 shows the procedure applied for different ages and the result for the entire range of ages and metallicities. The calculated RC colours and magnitudes, morphological age indices (see next section) and their uncertainties are presented in Tabs. A1 and A2, respectively. Detailed tables with those parameters and all other useful information concern-

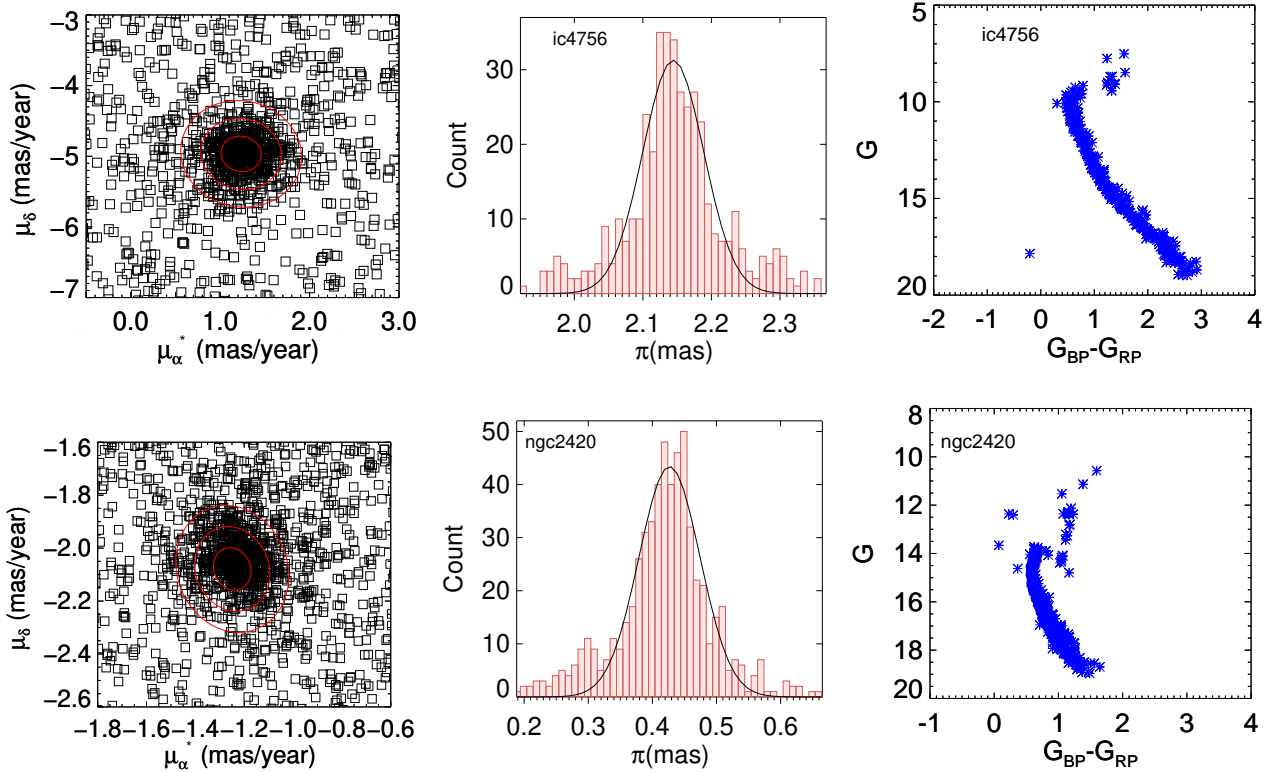


Figure 4. Left panels: Projection of the fitted 2D Gaussian function over the VPD, where the red ellipses represent the two-dimensional dispersion in the 1, 2 and 3- σ levels. Middle panels: one-dimensional Gaussian fit over the parallax values for the proper motion filtered sample. Right panels: CMD with *Gaia* passbands built from the final memberlist restricted by proper motion and parallax. In the examples, the OCs represented are: IC 4756 (top) and NGC 2420 (bottom).

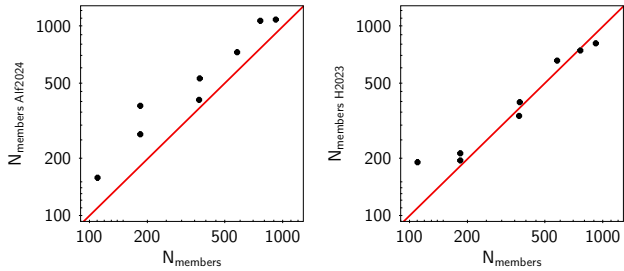


Figure 5. Comparison between the number of members obtained in this work (x-axis) with the literature (y-axis) for a sample of OCs within 1kpc. Left panel: comparison with Alf2024 results. Right panel: comparison with H2023 results.

ing our OC sample and also the calculations performed on the models are available electronically through Vizier².

6 RESULTS AND DISCUSSION

6.1 The RC position

From the mean values of colour and magnitude for RC stars identified in Sect 5, we obtained their absolute values. We took distances and colour excesses from D2021 to obtain the

distance modulus and the interstellar extinction for each passband. To convert colour excesses values into interstellar extinction, we used values from the relationship A_V/A_λ based on an established extinction law (Cardelli et al. 1989), with $R_V = 3.1$. Using these values, we obtained the absolute RC magnitudes M_G and M_K and intrinsic colour indices $(G_{BP} - G_{RP})_0$ and $(J - K)_0$.

We verified the variation of the RC absolute magnitude and intrinsic colour as a function of age, as can be seen in Fig. 8. We noted that for both visible (*Gaia*, upper panels) and infrared filters (2MASS, lower panels), RC stars tend to get significantly dimmer with age, within $8.3 < \log[t(\text{yr})] < 9.0$. Through this age interval, according to *Gaia* filters, the RC colour index seems not to change significantly, on the other hand, according to the infrared filters, the RC tends to get hotter. From $\log[t(\text{yr})] \sim 9.0$ onwards, for both visible and infrared filters, the RC tend to become cooler and a slightly brighter until the age of $\log[t(\text{yr})] \sim 9.2$. For older OCs, the values of M_G and M_K tend to remain approximately constant, but M_K is less affected by metallicity and exhibits a tighter distribution for older RC populations. On average the RC position tends to become cooler with age, in agreement with the PARSEC models and the analysis in Grocholski & Sarajedini (2002) for infrared bands.

The main structures formed in observational HR diagrams of field stars have already been pointed out in the literature (see Fig. 10 from Gaia Collaboration et al. (2018)).

² <http://cdsarc.u-strasbg.fr/vizier/cat/J/MNRAS/vol/page>

Table 4. Astrometric parameters obtained from our OCs memberlists.

Cluster	l degrees	b degrees	r_{lim} arcmin	r_{50} degress	μ_{α}^* mas/year	$\sigma_{\mu_{\alpha}^*}$ mas/year	μ_{δ} mas/year	$\sigma_{\mu_{\delta}}$ mas/year	ϖ mas	σ_{ϖ} mas	N
NGC 188	122.832	22.372	26.0	0.109	-2.323	0.095	-1.018	0.114	0.549	0.031	820
NGC 752	136.884	-23.343	79.7	0.399	9.779	0.225	-11.83	0.224	2.307	0.041	183
NGC 1245	146.653	-8.908	15.7	0.078	0.470	0.088	-1.662	0.068	0.335	0.046	641
NGC 1817	186.201	-13.021	22.1	0.166	0.424	0.082	-0.934	0.078	0.61	0.036	419
NGC 2099	177.611	3.08	29.6	0.123	1.882	0.155	-5.617	0.140	0.712	0.043	1541
Trumpler 5	202.816	1.000	24.0	0.120	-0.617	0.154	0.271	0.144	0.336	0.098	3593
Collinder 110	209.612	-1.868	27.5	0.138	-1.097	0.093	-2.045	0.096	0.472	0.050	1030
NGC 2354	238.391	-6.825	26.9	0.112	-2.862	0.085	1.860	0.090	0.812	0.026	234
NGC 2355	203.385	11.830	26.9	0.090	-3.841	0.077	-1.065	0.083	0.563	0.042	356
NGC 2360	229.799	-1.403	40.8	0.170	0.376	0.138	5.623	0.136	0.955	0.037	715
NGC 2423	230.507	3.563	43.3	0.253	-0.750	0.116	-3.586	0.120	1.098	0.030	367
NGC 2420	198.107	19.642	17.4	0.072	-1.221	0.077	-2.048	0.074	0.427	0.047	550
NGC 2447	240.063	0.146	37.4	0.156	-3.572	0.130	5.086	0.140	1.028	0.032	657
NGC 2477	253.547	-5.817	33.7	0.168	-2.430	0.163	0.899	0.170	0.722	0.029	2548
NGC 2527	246.108	1.882	34.7	0.231	-5.566	0.134	7.338	0.146	1.603	0.029	183
NGC 2539	233.721	11.114	25.0	0.146	-2.329	0.105	-0.538	0.100	0.798	0.033	421
NGC 2660	265.934	-3.011	13.5	0.045	-2.740	0.090	5.202	0.083	0.371	0.044	559
NGC 2682	215.653	31.909	37.5	0.219	-10.964	0.184	-2.922	0.179	1.193	0.04	912
IC 2714	292.397	-1.776	25.3	0.147	-7.585	0.145	2.691	0.158	0.774	0.036	1001
NGC 3960	294.377	6.174	15.2	0.076	-6.520	0.085	1.876	0.083	0.453	0.039	472
NGC 4337	299.316	4.559	22.1	0.074	-8.855	0.064	1.500	0.079	0.415	0.04	373
NGC 4349	299.737	0.828	23.6	0.118	-7.845	0.134	-0.265	0.144	0.557	0.047	1052
Collinder 261	301.712	-5.560	17.4	0.087	-6.369	0.129	-2.682	0.132	0.375	0.067	2374
NGC 5822	321.525	3.730	55.0	0.321	-7.485	0.185	-5.491	0.171	1.239	0.034	577
NGC 6134	334.922	-0.200	25.8	0.129	2.145	0.174	-4.446	0.159	0.912	0.048	752
NGC 6253	335.454	-6.254	18.2	0.091	-4.555	0.119	-5.288	0.113	0.624	0.043	778
IC 4651	340.093	-7.884	30.6	0.178	-2.438	0.194	-5.049	0.180	1.100	0.036	758
NGC 6583	9.273	-2.545	8.7	0.043	1.326	0.082	0.095	0.074	0.443	0.036	182
IC 4756	36.407	5.345	69.4	0.405	1.267	0.215	-4.955	0.238	2.144	0.046	370
NGC 6705	27.329	-2.786	23.1	0.135	-1.550	0.192	-4.172	0.187	0.426	0.112	3323
Ruprecht 147	20.919	-12.779	77.8	0.519	-0.869	0.309	-26.701	0.468	3.299	0.064	111
NGC 6811	79.221	11.998	37.4	0.156	-3.349	0.096	-8.805	0.101	0.905	0.027	287
NGC 6819	73.985	8.479	22.1	0.074	-2.896	0.097	-3.867	0.108	0.400	0.038	1754
NGC 7789	115.524	-5.371	35.9	0.150	-0.915	0.126	-1.958	0.131	0.507	0.036	3233

For example, the secondary red clump (SRC) is a structure more extended in its bluest part towards fainter magnitudes than the RC. It tends to appear around $(G_{BP} - G_{RP})_0 = 1.10$, $M_G = 0.60$ in observational *Gaia* HR diagrams, which corresponds to younger more massive RC stars. Indeed, the RC magnitude and colour from our observed sample reflect such extended structure. In the left panels of Fig. 8 we see this structure in *Gaia* passbands around the expected position and in 2MASS passbands this structure is more remarkable and lies around $(J - K)_0 = 0.53$, $M_K = -1.30$. According to our data, those RC stars are comprised in the age range of $8.80 < \log[t(\text{yr})] < 9.20$.

A bluer and vertical structure that is called the Vertical Red Clump (VRC) is also present, in which core-helium burning stars that are even more massive are more luminous than the RC and lie still on the blue part of it. This structure is present in the left panels of 8, for OCs younger than $\log[t(\text{yr})] = 8.80$ where the absolute magnitude decreases strongly with age.

In general, for both visible and infrared wavelengths, the values of M_G and M_K as a function of age are well represented by PARSEC isochrones (second column of panels in Fig. 8), especially for the older RC population (Onozato et al. 2019; Ruiz-Dern et al. 2018). We note that the infrared

models tend to present values of M_K systematically brighter for objects younger than $\log[t(\text{yr})] \sim 9.0$, as seen in the Figs. 6 and 7 from van Helshoecht & Groenewegen (2007).

When comparing the RC colour indices (third column of panels in Fig. 8), we noticed that the nearly solar metallicity models represent well the population older than $\log[t(\text{yr})] \sim 9.0$. On the other hand, they are systematically redder than the observed younger OCs. The RC colours, according to PARSEC isochrones, also exhibit a minimum at $\log[t(\text{yr})] \sim 9.0$ for metallicities $[Fe/H] \gtrsim -0.2$, however this trend is better followed by infrared data compared with visible data (right panels of Fig. 8). This discrepancy with the models was already noted in Piatti et al. (1998) and can also be observed in recent works with objects of age $\log[t(\text{yr})] \lesssim 8.8$ (Piatti et al. 2011; Holanda et al. 2022; Martinez et al. 2020; Bossini et al. 2019), in which the theoretical isochrones, when well fitted to the MS, do not pass through the RC stars, predicting a RC locus systematically redder. Such discrepancies may be caused by a combination of effects such as: unresolved binary stars, mass distribution of giant parent clump stars (including mass loss), differential reddening or the presence of SRC stellar populations simultaneously with the RC for some objects, making the observed average RC value bluer. Alternatively, this may indicate that

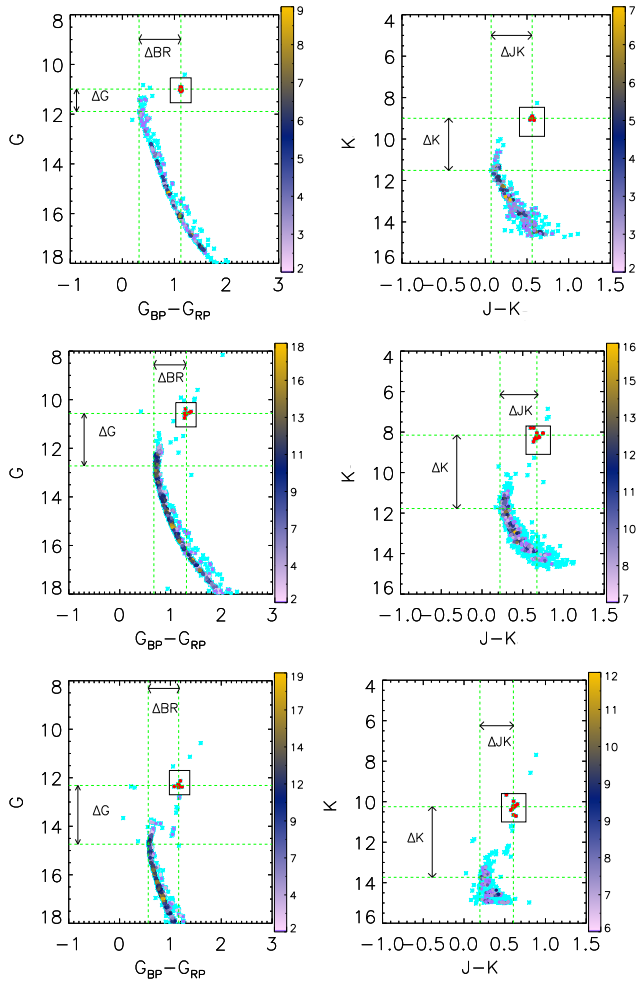


Figure 6. The method used to determine the colour and magnitude for the RC and turnoff positions. Left: CMDs with *Gaia* passbands of the OCs NGC 6811 (top), IC 4651 (middle) and NGC 2420 (bottom). Right: 2MASS CMDs for the same OCs. Cyan symbols represent excluded stars with few neighbours, the blue and yellow symbols represent the density and the colour bar the number of close neighbours. The black box represents the region used to select RC candidates and the red filled circles identify the RC stars, whose mean magnitude and colour were measured. Green dotted lines mark the RC and turnoff positions. The measured indices are also indicated.

the models still have deficiencies in bolometric corrections, colour transformations and effective temperatures in this age range (Girardi 1999; An et al. 2019; Sandquist et al. 2020).

Our sample of clusters has approximately solar metallicity, with an average value of $[Fe/H] = 0.02$ and $\sigma_{[Fe/H]} = 0.12$ dex, with few clusters outside this range. We note that OCs with metallicities that are more discrepant from the average tend to present large variations in RC colour, but more moderate variations in magnitude, mainly for the infrared, in agreement with the expectation that the average RC magnitude is a good indicator of distance even with variations in metallicity.

We also determined the average RC magnitude for our sample by adopting an interval of ages less affected by population effects. For this purpose, we used objects older than $\log[t(\text{yr})] = 9.2$, a similar value adopted in Grocholski &

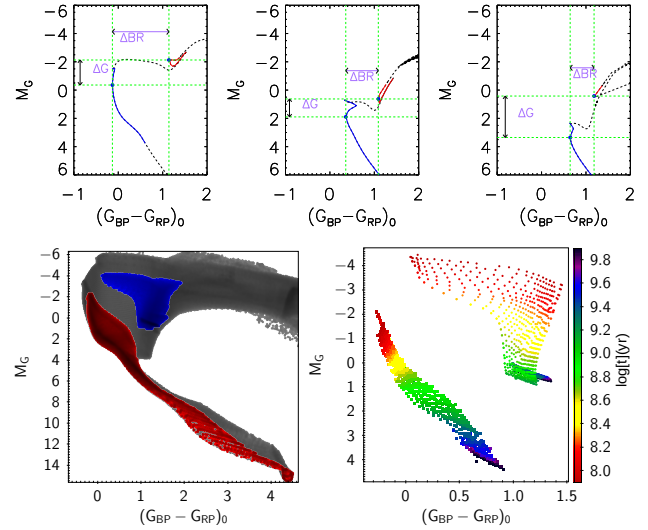


Figure 7. Top: Examples of the method used to determine the colour and magnitude for RC and turnoff for solar metallicity PARSEC isochrones of age $\log[t(\text{yr})] = 8.3$ (left), 9.1 (middle) and 9.5 (right). Bottom left panel: CMD of all isochrones used, where the red region corresponds to MS stars ($\text{label}=1$) and the blue region corresponds to the beginning of the RC phase ($\text{label}=4,5,6$). Bottom right panel: RC and turnoff positions identified from the models, where the colourbar indicates the ages.

Table 5. RC average values calculated for M_G and M_K from this work and from the literature: Ruiz-Dern et al. (2018) (RD2018), Hawkins et al. (2017) (H2017), van Helshoecht & Groenewegen (2007) (vH2007) and Grocholski & Sarajedini (2002) (Gro2002).

Source	M_G	M_K
This work	0.42 ± 0.05	-1.66 ± 0.04
RD2018	0.495 ± 0.009	-
H2017	0.44 ± 0.01	-1.61 ± 0.01
vH2007	-	-1.57 ± 0.05
Gro2002	-	-1.61 ± 0.04

Sarajedini (2002) to estimate the mean RC value for M_K . We found $M_G = 0.42 \pm 0.05$ and $M_K = -1.66 \pm 0.04$, which is in good agreement with the literature (Table 5).

6.2 Morphological age indices

In this section, we investigated how turnoff-RC differences relate to age and metallicity. Using the quantities determined in Section 5, we determined the indices ΔG and ΔK as the difference in magnitude between the RC and the turnoff, as well as the colour difference ΔBR and ΔJK for both *Gaia* and 2MASS passbands, respectively.

The top panels of Fig. 9 show how the indices ΔG and ΔBR are related with age and metallicity and the bottom ones illustrate the same relations for ΔK and ΔJK indices. It is evident that there appear to be two approximate linear relationships of ΔG with $\log[t(\text{yr})]$: one for objects with ages younger than $\log[t(\text{yr})] \sim 8.8$ and another for objects older than this limit. Our older OCs present a similar linear trend

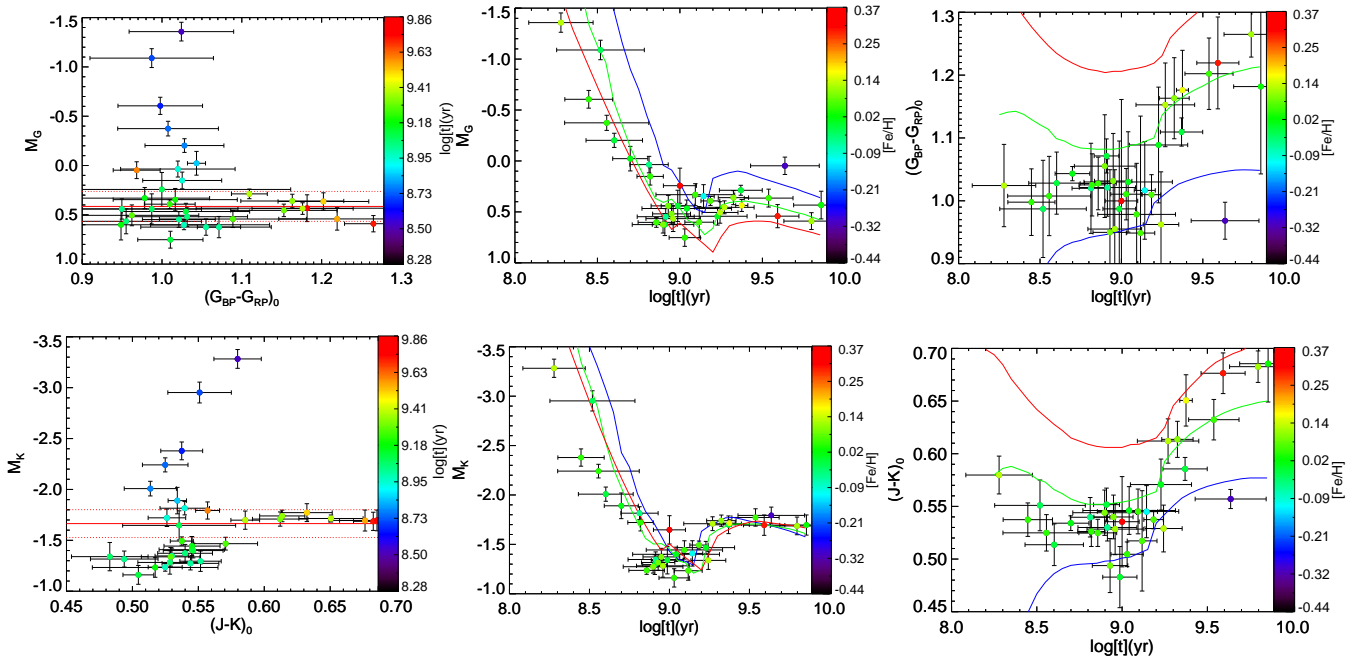


Figure 8. RC colours and average magnitudes from our OC sample. Top panels: *Gaia* DR3 bands. Bottom panels: 2MASS bands. The first column presents colour properties and mean magnitude in addition to the mean value (solid red line) and standard deviation (dotted red lines) of the clump magnitude for $\log[t(\text{yr})] > 9.2$ and the colour bar represents the cluster age. The second column exhibits the relationship between age and average RC magnitude, while the third column of panels shows the relationship between age and average RC colour. For the second and third column of panels, the colour bars represent the metallicity and the lines represent the RC predictions according to PARSEC models for three different metallicity values: maximum metallicity of the cluster sample (red), minimum metallicity (blue) and solar metallicity (green). The error bars in absolute magnitudes and intrinsic colors were determined by error propagation.

to that determined by Phelps et al. (1994) for the indices in the planes $\delta_1(BV)$ vs δV and $\delta_1(VI)$ vs δV .

At least in the range spanned by OCs in our sample, metallicity does not appear to affect strongly the ΔG values for $\log[t(\text{yr})] > 9.0$, which has already been verified by other authors (Phelps et al. 1994; Carraro & Chiosi 1994; Salaris et al. 2004; Beletsky et al. 2009). This effect is confirmed by the overplotted PARSEC models.

According to our data and the PARSEC models, the index ΔBR also shows little dependence on metallicity for objects older than $\log[t(\text{yr})] \sim 8.8$. The models indicate a more significant dependence on metallicity for younger objects (see Fig. 9, top-right panel).

In general, the models show good agreement with the data on the relation ΔG versus $\log[t(\text{yr})]$. Regarding the values of ΔBR , apparently for younger objects ($\log[t(\text{yr})] < 8.8$), the isochrones tend to overestimate this index, which is related to the prediction of redder RC in this age interval (see Sect. 6.1).

Regarding the infrared indices ΔK and ΔJK (bottom panels in Fig. 9), it is possible to note trends analogous to those for *Gaia* indices, but both indices present a wider distribution when compared with *Gaia* ones due to the larger photometric errors. In general, PARSEC models show good agreement with the data for the relation ΔK versus $\log[t(\text{yr})]$. However, the index ΔJK seems to be much more affected by the 2MASS colour indices errors, especially for older OCs ($\log[t(\text{yr})] \gtrsim 9.0$), which present a distribution within $0.4 < \Delta JK < 0.5$. The difference ΔJK of our OCs exhibits a range of ~ 0.35 mag (considering the overall

age interval), although the average error of the colour index $(J - K)$ for our clusters members are about ~ 0.05 mag. We did not see the same problem with *Gaia* photometry with the index ΔBR , because this index from our OCs star members spreads over a wider range (~ 1 mag), where the mean colour index $(G_{BP} - G_{RP})$ error is about ~ 0.008 mag, in other words this index is not very affected by photometric errors.

We also calculated a similar age index to MAR, defined in Anthony-Twarog & Twarog (1985), taking the ratio $\Delta G / \Delta BR$. We do not define the same index for 2MASS bands due to the scatter observed in index ΔJK . The same ratio was determined for PARSEC isochrones and a comparison with data is shown in Fig. 10. Despite the discrepancies of the index ΔBR for younger OCs, the index MAR is very well reproduced by PARSEC isochrones, with the exception of OCs older than $\log[t(\text{yr})] > 9.5$. In Anthony-Twarog & Twarog (1985) a linear correlation with age is obtained from MAR (ratio $\Delta V / \Delta(B - V)$) for objects older than 2 Gyr ($\log[t(\text{yr})] = 9.3$), however, our work shows that this relation is clearly non-linear, especially for objects younger than 1 Gyr and older than 3 Gyr.

6.3 Age calibrations

As far as we are aware, age calibrations for *Gaia* data (ΔG and ΔBR indices) are not yet available in the literature, so here we will provide them for both *Gaia* morphological indices for the first time. We also performed calibrations for the ΔK index as a benchmark. In Fig. 9 it is possible to

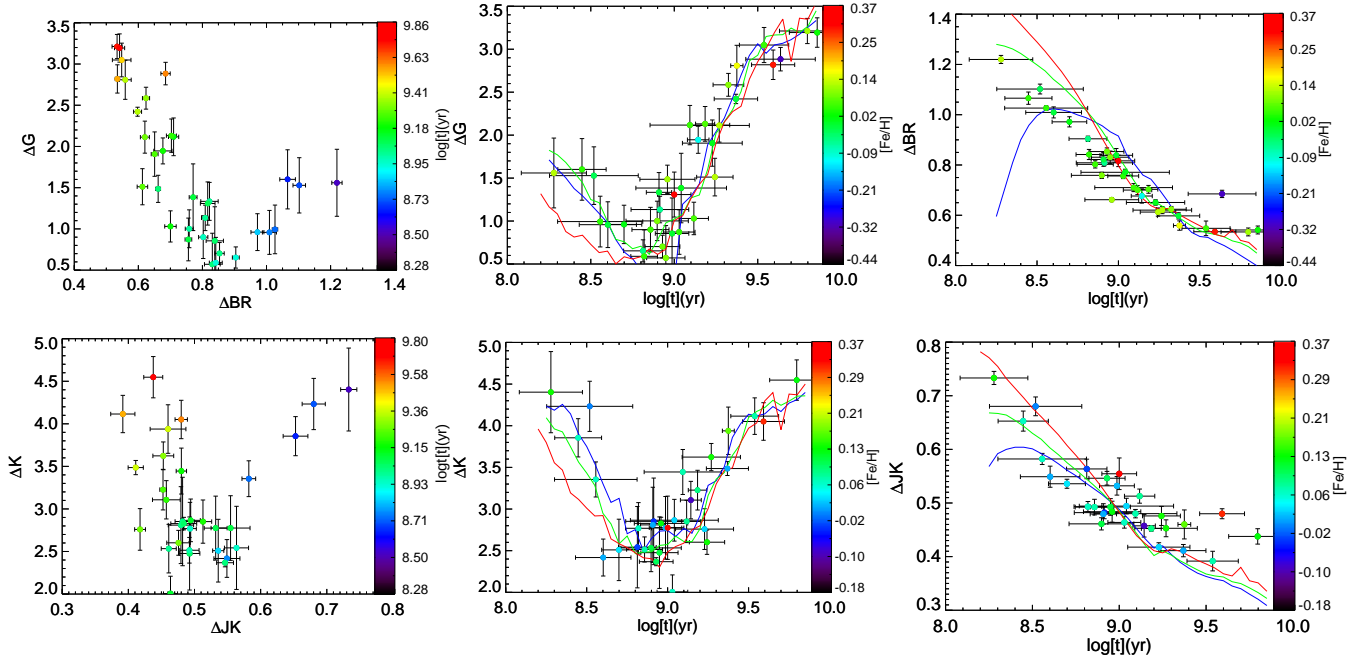


Figure 9. Age evolution of morphological colour indices. Top panels: *Gaia* DR3 indices. Bottom panels: Same, but for 2MASS indices. The first column presents the differences in colour and magnitude from the RC and turnoff positions, the colour bar represents age. The second column represents the relationship between the indices ΔG versus age (top) and ΔK versus age (bottom), while the third column represents the relationship between the indices ΔBR versus age (top) and ΔJK versus age (bottom). For the second and third column of panels the colour bars represent the metallicity and the lines indicate the indices predictions according to PARSEC models for three different metallicities: maximum metallicity of the cluster sample (blue), minimum metallicity (red) and solar metallicity (green). The error bars are also represented.

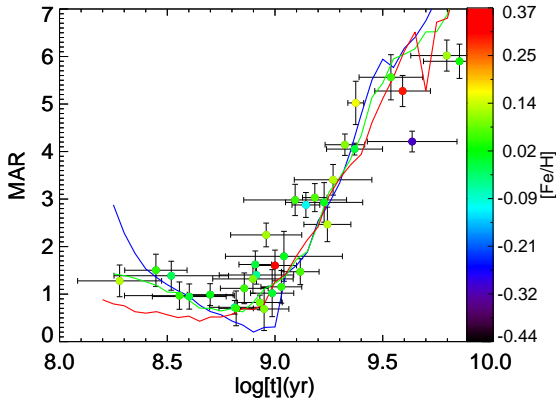


Figure 10. The evolution of the morphological age index MAR. The colour bar represents the metallicity. The lines represent the same index predicted by PARSEC models for three different metallicity values: maximum metallicity of the cluster sample (red), minimum metallicity (blue) and solar metallicity (green). The error bars were determined by propagating the errors from the ratio $\Delta G/\Delta BR$.

note that both indices ΔG and ΔK increase with age for OCs older than $\log[t(\text{yr})] = 8.8$, for which we determined calibrations (Eqs. 5 and 6) similar to those present in Beletsky et al. (2009). In addition, we determined two more calibrations for ΔG : quadratic in ΔG (Eq. 7) and a relation that takes into account the metallicity (Eq. 8). Fig. 11 summarizes all these calibrations. Mean residuals, correlation

Table 6. Mean residuals and correlation coefficients of the calibration equations established in this work. The age range in which each equation are calculated, and therefore applicable are also indicated.

Eq.	Residuals	Correlation	Validity range
5	0.09	0.92	$8.8 < \log[(\text{yr})] < 9.9$
6	0.10	0.85	$8.8 < \log[(\text{yr})] < 9.9$
7	0.08	0.95	$8.8 < \log[(\text{yr})] < 9.9$
8	0.09	0.92	$8.8 < \log[(\text{yr})] < 9.9$
9	0.06	0.98	$8.3 < \log[(\text{yr})] < 9.9$

coefficients and the age range of the calibration equations established in this work are present in Table 6.

$$\log[t(\text{yr})] = 8.63(\pm 0.05) + 0.31(\pm 0.03) \times \Delta G \quad (5)$$

$$\log[t(\text{yr})] = 8.12(\pm 0.13) + 0.33(\pm 0.04) \times \Delta K \quad (6)$$

$$\log[t(\text{yr})] = 8.89(\pm 0.10) - 0.01(\pm 0.13) \times \Delta G + 0.07(\pm 0.04) \times (\Delta G)^2 \quad (7)$$

$$\log[t(\text{yr})] = 8.63(\pm 0.05) + 0.31(\pm 0.03) \times \Delta G - 0.02(\pm 0.15) \times [Fe/H] \quad (8)$$

Regarding the age calibration for the ΔK index (Eq. 6),

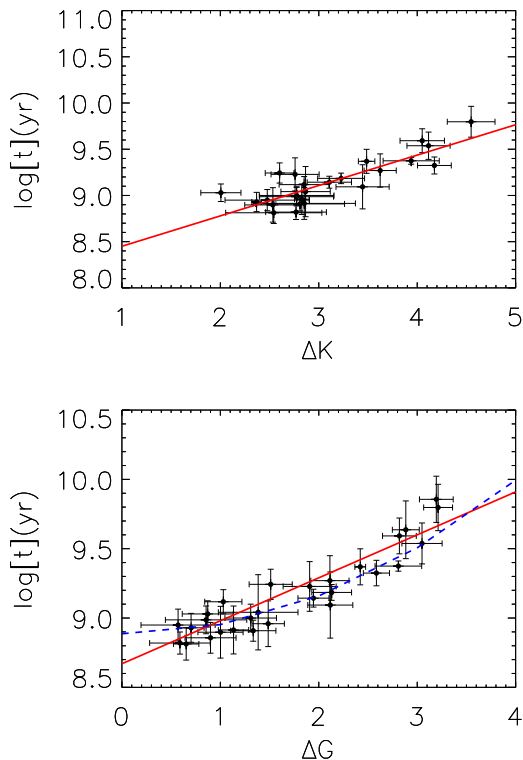


Figure 11. Top: Linear (red line) relation of $\log[t(\text{yr})]$ versus ΔK . Bottom: Linear (red line) and quadratic (blue dotted line) of the relation $\log[t(\text{yr})]$ versus ΔG .

we see a very good agreement with [Beletsky et al. \(2009\)](#), showing that our method provides similar results in comparison with those obtained by visual inspection of the CMDs, which validates its application on *Gaia* data. As seen in Sect. 6.2 and already evidenced by other authors for visible and infrared morphological age indices ΔV and ΔK ([Phelps et al. 1994](#); [Carraro & Chiosi 1994](#); [Salaris et al. 2004](#); [Beletsky et al. 2009](#)), the dependence of the index ΔG with metallicity is small (see Fig. 9), so that in many cases the metallicity term can be neglected. As accurate metallicity determinations are scarce in the literature, equations 5 and 7 become useful tools for determining ages of Galactic OCs whenever their turnoffs and RC positions are measured with good accuracy on their CMDs.

6.4 General formula

As seen in Fig. 9, when we took into account the relation $\log[t(\text{yr})]$ versus ΔG , we realize that objects with ages in the range $8.3 < \log[t(\text{yr})] < 8.8$ may have the same ΔG values as those of $8.8 < \log[t(\text{yr})] < 9.5$. However, the parameter ΔBR has an almost linear dependence on age, i.e., younger objects exhibit greater ΔBR than the older ones. In this case, using the index ΔBR breaks the degeneracy of the ΔG values as an age indicator. Thus, by extending the age calibration to the interval $\sim 8.3 < \log[t(\text{yr})] < 9.0$, we were able to establish a fitting function with quadratic and linear terms in both indices ΔG and ΔBR (Eq. 9 and Table 7). A comparison of OCs ages from our sample with

Table 7. Coefficients of Eq. 9.

Coef	Value
a	9.64 ± 0.34
b	-0.32 ± 0.09
c	0.14 ± 0.03
d	-0.81 ± 0.06

that determined using Eq. 9 is shown in Fig. 12, where we note small residuals. Therefore, Eq. 9 represents an important tool to determine OCs ages within a wide range using *Gaia* data.

$$\log[t(\text{yr})] = a + b \Delta G + c (\Delta G)^2 + d (\Delta BR)^2 \quad (9)$$

7 CONCLUSIONS

In this work we were able to obtain member star lists for a set of 34 star clusters from accurate astrometry and photometry from *Gaia* DR3 data using a uniform methodology. CMDs were constructed and morphological age indices were measured.

We presented an observational view of the RC population through the interval $8.3 < \log[t(\text{yr})] < 9.9$. In general, for both visible and infrared, the values of the absolute magnitudes of the RC, M_G and M_K as a function of age are well represented by PARSEC isochrones. We note that for the infrared the models tend to present values of M_K systematically brighter for younger objects.

When comparing the RC colour indices, we noticed that the models represent well the older population ($\log[t(\text{yr})] > 9.0$). However, they are systematically redder than observed younger OCs. The same conclusions were drawn by other authors for objects with age $\log[t(\text{yr})] \lesssim 8.8$ ([Piatti et al. 2011](#); [Holanda et al. 2022](#); [Martinez et al. 2020](#); [Bossini et al. 2019](#)). Such discrepancies may be caused by a combination of different effects. For example, the presence of unresolved binary stars, the mass distribution of the RC progenitors stars (including mass loss), presence of differential reddening, or the presence of SRC stellar populations simultaneously with the RC for some objects, making the observed average RC colour bluer than expected. Alternatively, this may indicate that the models still present limitations such as bolometric corrections, colour transformations and effective temperatures for this age range. Uncertainties of transformations from the theoretical to the observational plane also play a role.

Comparisons of the established morphological indices showed that the models tend to satisfactorily predict the ΔG index for the entire age range explored here. But for ages $\log[t(\text{yr})] < 8.8$, the models tend to present the index ΔBR systematically greater than observed (probably an effect caused by the inefficiency of predicting the RC colours for younger ages. According to our data, the models also face challenges in accurately predicting the index ΔBR for older objects ($\log[t(\text{yr})] > 9.6$), although few OCs are that old to provide a useful comparison.

Finally, we provided a set of age calibration functions based on *Gaia* morphological indices for the first time, al-

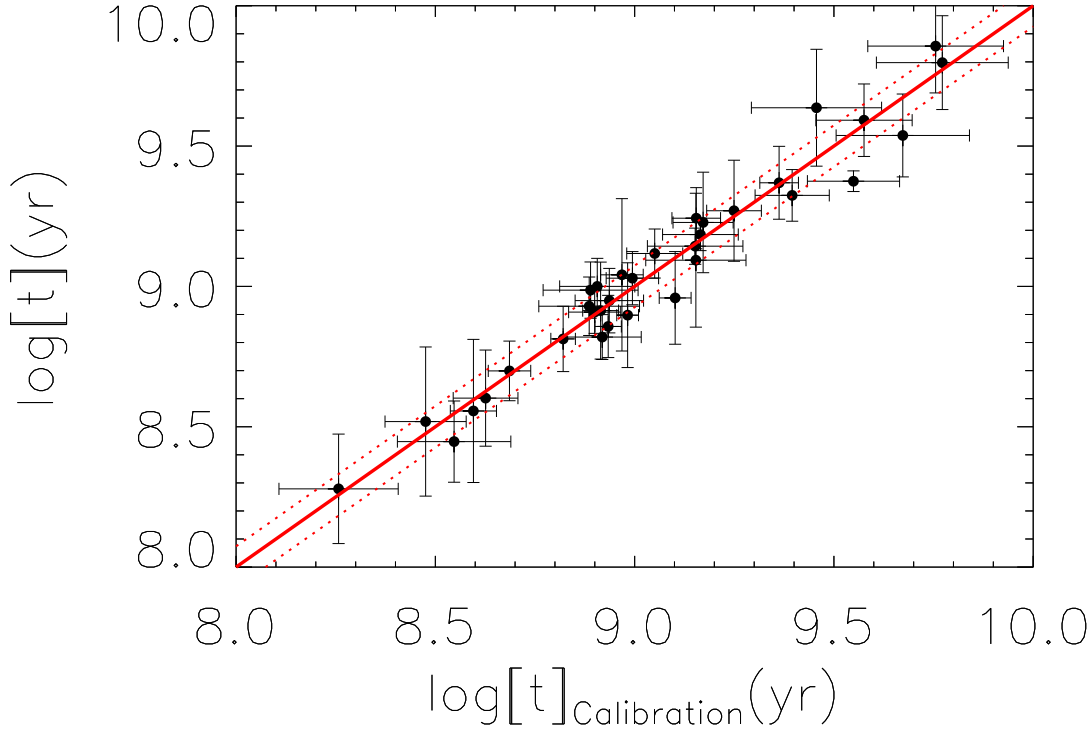


Figure 12. Relation between ages of OCs from the literature as function of their ages determined from Eq. 9. The continuous line gives a linear fit to the relation and the dashed lines correspond to its $1 - \sigma$ uncertainties. The relation is given by $\log[t(\text{yr})] = A \times \log t_{\text{fit}} + B$, where $A=1.00$ and $B=0.00$. The error bars in the X axis were determined by error propagating from Eq. 9 and the Y axis are errors in $\log[t(\text{yr})]$ from the literature.

lowing an estimate of star cluster ages based on such indices. In particular, a non-linear fitting function was obtained by using both indices ΔBR and ΔG , extending the age determination using such method to younger objects. We have demonstrated its accuracy for the range $8.3 < \log[t(\text{yr})] < 9.8$ by a direct comparison with ages from the literature, obtaining a mean residuals of 0.06 dex in $\log[t(\text{yr})]$.

Although out the scope of the present paper, asteroseismology is an alternative approach to obtain precise ages of OCs, from which new color calibrations can be derived. However, due to the lack of OCs with ages measured via asteroseismology (e.g. Brogaard et al. 2023; Ash et al. 2025), we still face difficulties incorporating a significant number of objects with isochrone-independent age measurements. In the future, as a sizeable sample of stars in several clusters is measured using asteroseismology, the results from this age-dating method may then be used to establish new color calibrations.

ACKNOWLEDGEMENTS

We thank the referee for a critical, positive and motivating report. The authors wish to thank the Brazilian financial agencies FAPEMIG, CNPq and CAPES (finance code 001). W.Corradi acknowledges the support from CNPq - BRICS 440142/2022-9, FAPEMIG APQ 02493-22 and FNDCT/FINEP/REF 0180/22. F.F.S.M. acknowledges fi-

ancial support from Conselho Nacional de Desenvolvimento Científico e Tecnológico – CNPq (proc. 404482/2021-0) and from FAPERJ (proc. E-26/201.386/2022 and E-26/211.475/2021). This research has made use of the VizieR catalogue access tool, CDS, Strasbourg, France. This work has made use of data from the European Space Agency (ESA) mission *Gaia* (<https://www.cosmos.esa.int/gaia>), processed by the *Gaia* Data Processing and Analysis Consortium (DPAC, <https://www.cosmos.esa.int/web/gaia/dpac/consortium>). Funding for the DPAC has been provided by national institutions, in particular the institutions participating in the *Gaia* Multilateral Agreement. This research has made use of TOPCAT (Taylor 2005).

DATA AVAILABILITY

The data underlying this article is publicly available (*Gaia DR3* and 2MASS) or is available in the article.

REFERENCES

- Alfonso J., García-Varela A., Vieira K., 2024, *A&A*, **689**, A18
 An D., Pinsonneault M. H., Terndrup D. M., Chung C., 2019, *ApJ*, **879**, 81
 Angelo M. S., Santos J. F. C., Corradi W. J. B., Maia F. F. S., 2019, *A&A*, **624**, A8

- Angelo M. S., Corradi W. J. B., Santos J. F. C. J., Maia F. F. S., Ferreira F. A., 2021, *MNRAS*, **500**, 4338
- Anthony-Twarog B. J., Twarog B. A., 1985, *ApJ*, **291**, 595
- Ash A. L., Pinsonneault M. H., Vradar M., Zinn J. C., 2025, *ApJ*, **979**, 135
- Battinelli P., Brandimarti A., Capuzzo-Dolcetta R., 1994, *A&AS*, **104**, 379
- Beletsky Y., Carraro G., Ivanov V. D., 2009, *A&A*, **508**, 1279
- Bilir S., Önal Ö., Karaali S., Cabrera-Lavers A., Çakmak H., 2013, *Ap&SS*, **344**, 417
- Bossini D., et al., 2019, *A&A*, **623**, A108
- Bressan A., Marigo P., Girardi L., Salasnich B., Dal Cero C., Rubele S., Nanni A., 2012, *MNRAS*, **427**, 127
- Brogaard K., et al., 2023, *A&A*, **679**, A23
- Cantat-Gaudin T., et al., 2018, *A&A*, **618**, A93
- Cantat-Gaudin T., et al., 2020, *A&A*, **640**, A1
- Cardelli J. A., Clayton G. C., Mathis J. S., 1989, *ApJ*, **345**, 245
- Carraro G., Chiosi C., 1994, *A&A*, **287**, 761
- Carraro G., Geisler D., Villanova S., Frinchaboy P. M., Majewski S. R., 2007, *A&A*, **476**, 217
- Castro-Ginard A., et al., 2020, *A&A*, **635**, A45
- Chen Y. Q., Zhao G., 2020, *MNRAS*, **495**, 2673
- Dias W. S., Monteiro H., Moitinho A., Lépine J. R. D., Carraro G., Paunzen E., Alessi B., Vilella L., 2021, *Monthly Notices of the Royal Astronomical Society*, **504**, 356
- Dürbeck W., 1960, *Z. Astrophys.*, **49**, 214
- Evans D. W., et al., 2018, *A&A*, **616**, A4
- Ferreira F. A., Santos J. F. C., Corradi W. J. B., Maia F. F. S., Angelo M. S., 2019, *MNRAS*, **483**, 5508
- Ferreira F. A., Corradi W. J. B., Maia F. F. S., Angelo M. S., Santos J. F. C. J., 2020, *MNRAS*, **496**, 2021
- Ferreira F. A., Corradi W. J. B., Maia F. F. S., Angelo M. S., Santos J. F. C. J., 2021, *MNRAS*, **502**, L90
- Friel E. D., 1995, *ARA&A*, **33**, 381
- Gaia Collaboration et al., 2018, *A&A*, **616**, A10
- Gaia Collaboration et al., 2021, *A&A*, **649**, A1
- Gaia Collaboration et al., 2023, *A&A*, **674**, A1
- Geisler D., Bica E., Dottori H., Clariá J. J., Piatti A. E., Santos Joao F. C. J., 1997, *AJ*, **114**, 1920
- Girardi L., 1999, *MNRAS*, **308**, 818
- Girardi L., 2016, *ARA&A*, **54**, 95
- Grocholski A. J., Sarajedini A., 2002, *AJ*, **123**, 1603
- Hawkins K., Leistedt B., Bovy J., Hogg D. W., 2017, *Monthly Notices of the Royal Astronomical Society*, **471**, 722
- He Z., Liu X., Luo Y., Wang K., Jiang Q., 2022, arXiv e-prints, p. arXiv:2209.08504
- Holanda N., Ramos A. A., Peña Suárez V. J., Martínez C. F., Pereira C. B., 2022, *Monthly Notices of the Royal Astronomical Society*, **516**, 4484
- Hunt E. L., Reffert S., 2023, *A&A*, **673**, A114
- Im H., Kim S. C., Kyeong J., Park H. S., Lee J. H., 2023, *AJ*, **165**, 53
- Kharchenko N. V., Piskunov A. E., Röser S., Schilbach E., Scholz R. D., 2005, *A&A*, **438**, 1163
- Kharchenko N. V., Piskunov A. E., Schilbach E., Röser S., Scholz R. D., 2013, *A&A*, **558**, A53
- Lada C. J., Lada E. A., 2003, *ARA&A*, **41**, 57
- Lindgren L., et al., 2018, *A&A*, **616**, A2
- Lindgren L., et al., 2021, *A&A*, **649**, A2
- Liu L., Pang X., 2019, *ApJS*, **245**, 32
- Loktin A. V., Popova M. E., 2017, *Astrophysical Bulletin*, **72**, 257
- Martínez C. F., Holanda N., Pereira C. B., Drake N. A., 2020, *Monthly Notices of the Royal Astronomical Society*, **494**, 1470
- Netopil M., Paunzen E., Heiter U., Soubiran C., 2016, *A&A*, **585**, A150
- Onozato H., Ita Y., Nakada Y., Nishiyama S., 2019, *MNRAS*, **486**, 5600
- Oralhan İ. A., Karataş Y., Schuster W. J., Michel R., Chavarría C., 2015, *New Astron.*, **34**, 195
- Parisi M. C., et al., 2014, *AJ*, **147**, 71
- Phelps R. L., Janes K. A., Montgomery K. A., 1994, *AJ*, **107**, 1079
- Piatti A. E., Clariá J. J., Bica E., 1998, *ApJS*, **116**, 263
- Piatti A. E., Clariá J. J., Ahumada A. V., 2010, *Monthly Notices of the Royal Astronomical Society*, **402**, 2720
- Piatti A. E., Clariá J. J., Bica E., Geisler D., Ahumada A. V., Girardi L., 2011, *Monthly Notices of the Royal Astronomical Society*, **417**, 1559
- Riello M., et al., 2021, *A&A*, **649**, A3
- Ruiz-Dern L., Babusiaux C., Arenou F., Turon C., Lallement R., 2018, *A&A*, **609**, A116
- Salaris M., Weiss A., Percival S. M., 2004, *A&A*, **414**, 163
- Sandquist E. L., et al., 2020, *AJ*, **159**, 96
- Sim G., Lee S. H., Ann H. B., Kim S., 2019, *JKAS*, **52**, 145
- Skrutskie M. F., et al., 2006, *AJ*, **131**, 1163
- Taylor M. B., 2005, in Shopbell P., Britton M., Ebert R., eds, *ASPC Vol. 347, Astronomical Data Analysis Software and Systems XIV*. p. 29
- Zasowski G., et al., 2013, *AJ*, **146**, 64
- Zhang H., Chen Y., Zhao G., 2021, *ApJ*, **919**, 52
- van Helshoecht V., Groenewegen M. A. T., 2007, *A&A*, **463**, 559

APPENDIX A: TABLES

This appendix contains informations from OCs CMDs properties. In Table A1 the average RC apparent magnitudes (G and K) and colour indices ($(G_{BP} - G_{RP})$ and $\sigma_{(J-K)}$) and their uncertainties are presented. The number of RC stars N_G and N_K filtered by the box-shaped filter for *Gaia* and 2MASS CMDs is also presented. In Table A2 the morphological age indices ΔG , ΔBR , ΔK and ΔJK and their uncertainties are presented. A review of the astrophysical parameters for the cluster NGC2354 taken from the literature is presented in Table A3.

A1 The NGC2354 age

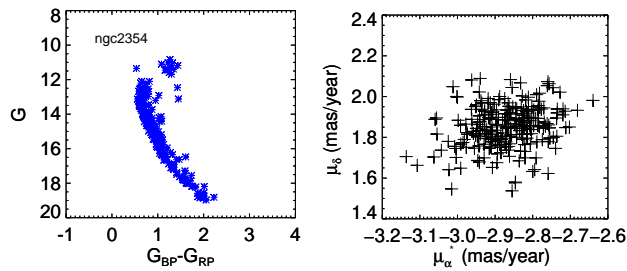
NGC2354 is an OC located in the constellation of Canis Major which, according to our analysis from *Gaia* data, has an apparent diameter of 25 arcmin and 234 members. Our analysis proved to be efficient in obtaining reliable members of this cluster, as its CMD clearly presents an evolutionary sequence without many *outliers* (see Fig. A1) and the dispersion values of the members in astrometric space were compatible with those of the other clusters with similar distances (see Table 4).

However, we note that the age value used in this work (established in N2016) proved to be underestimated in relation to recent age values established in the literature, based on determinations with data from *Gaia*. We also noticed discrepancies in the properties presented by this cluster when compared to others. This object presented very discrepant values on the plane ΔG versus ΔBR and in the age relation of the MAR index, when compared to objects with the same age, as can be seen in Figure A2. This reinforces the importance of such indices in characterizing OCs morphologically.

We carried out a review of the astrophysical parameters of this object in the literature and noticed that in studies where the authors did not use precise proper motion data, low age values were assigned to this object (see Table A3).

Table A1. Average RC apparent magnitudes and colour indices and their uncertainties. The number of RC stars filtered by the box-shaped filter for *Gaia* and 2MASS CMDs is also presented.

OC	G	σ_G	$(G_{BP} - G_{RP})$	$\sigma_{(G_{BP} - G_{RP})}$	K	σ_K	$(J - K)$	$\sigma_{(J - K)}$	N_G	N_K
NGC 188	12.13	0.07	1.37	0.02	9.69	0.08	0.72	0.01	14.0	15.0
NGC 752	8.90	0.06	1.16	0.01	6.77	0.06	0.60	0.01	14.0	14.0
NGC 1245	13.65	0.03	1.38	0.01	11.14	0.05	0.65	0.01	41.0	44.0
NGC 1817	12.15	0.05	1.35	0.01	9.73	0.05	0.66	0.01	26.0	28.0
NGC 2099	10.96	0.05	1.42	0.01	8.44	0.06	0.69	0.01	27.0	26.0
Trumpler 5	14.30	0.02	1.88	0.01	11.01	0.03	0.91	0.01	92.0	110.0
Collinder 110	13.20	0.04	1.72	0.01	10.25	0.04	0.83	0.01	43.0	45.0
NGC 2354	11.29	0.07	1.25	0.03	9.15	0.11	0.64	0.02	12.0	12.0
NGC 2355	12.16	0.09	1.22	0.01	10.01	0.09	0.61	0.01	8.0	10.0
NGC 2360	10.92	0.05	1.21	0.01	8.76	0.06	0.62	0.01	12.0	13.0
NGC 2423	10.70	0.05	1.19	0.0	8.59	0.06	0.60	0.01	11.0	11.0
NGC 2420	12.32	0.02	1.16	0.01	10.25	0.08	0.61	0.01	10.0	12.0
NGC 2447	9.90	0.06	1.08	0.01	8.01	0.07	0.53	0.02	12.0	14.0
NGC 2477	12.09	0.03	1.48	0.01	9.48	0.02	0.70	0.01	77.0	78.0
NGC 2527	9.23	0.06	1.12	0.01	7.21	0.06	0.58	0.01	4.0	4.0
NGC 2539	10.63	0.08	1.14	0.01	8.61	0.1	0.57	0.01	9.0	9.0
NGC 2660	13.93	0.03	1.60	0.01	11.05	0.04	0.77	0.01	31.0	31.0
NGC 2682	10.16	0.07	1.26	0.03	7.93	0.08	0.65	0.01	10.0	9.0
IC 2714	10.86	0.08	1.54	0.02	8.21	0.08	0.75	0.01	14.0	14.0
NGC 3960	12.92	0.07	1.47	0.02	10.37	0.08	0.67	0.01	12.0	12.0
NGC 4337	13.50	0.02	1.54	0.01	10.73	0.03	0.76	0.01	21.0	21.0
NGC 4349	11.10	0.07	1.57	0.02	8.30	0.09	0.78	0.01	9.0	9.0
Collinder 261	13.51	0.04	1.63	0.02	10.66	0.05	0.86	0.01	28.0	34.0
NGC 5822	10.43	0.04	1.25	0.01	8.19	0.05	0.62	0.01	17.0	17.0
NGC 6134	11.75	0.04	1.53	0.01	8.98	0.05	0.75	0.01	24.0	22.0
NGC 6253	12.32	0.05	1.58	0.01	9.52	0.05	0.82	0.01	20.0	20.0
IC 4651	10.57	0.03	1.31	0.01	8.15	0.06	0.67	0.01	10.0	12.0
NGC 6583	13.45	0.04	1.82	0.02	10.24	0.06	0.86	0.01	20.0	20.0
IC 4756	9.05	0.08	1.31	0.02	6.72	0.09	0.64	0.01	10.0	10.0
NGC 6705	11.24	0.04	1.68	0.01	8.27	0.06	0.84	0.01	27.0	26.0
Ruprecht 147	8.10	0.04	1.31	0.02	5.74	0.03	0.70	0.02	5.0	5.0
NGC 6811	10.99	0.03	1.12	0.01	9.00	0.03	0.56	0.01	6.0	6.0
NGC 6819	12.71	0.03	1.38	0.01	10.26	0.03	0.70	0.01	39.0	39.0
NGC 7789	12.64	0.02	1.47	0.01	10.03	0.02	0.72	0.01	105.0	104.0

**Figure A1.** Results of the membership assignment procedure for NGC 2354. Left: CMD of the most probable members. Right: VPD of the most probable members.

We note that prior to the availability of data from *Gaia*, the determinations of age, distance and colour excess, on average, were: $\log[t] = 8.35$ and $\sigma_{\log[t(\text{yr})]} = 0.27$, $\bar{d} = 3027$ pc and $\sigma_d = 915$ pc and $\overline{E(B - V)} = 0.31$ and $\sigma_{E(B - V)} = 0.17$. It is evident that the age value is compatible with the average established in N2016 of $\log[t(\text{yr})] = 8.30 \pm 0.23$. With the exception of [Kharchenko et al. \(2013\)](#), the other authors who characterized this cluster before the *Gaia* era,

used UVB photometry and interpreted its CMD as a much younger and more distant object.

After the availability of *Gaia*, the same determinations led to the following average values: $\log[t(\text{yr})] = 9.14$ and $\sigma_{\log[t(\text{yr})]} = 0.06$, $\bar{d} = 1259$ pc and $\sigma_d = 84$ pc and $\overline{E(B - V)} = 0.16$ and $\sigma_{E(B - V)} = 0.06$. A smaller fluctuation of the values and a better convergence of the distance estimate ($d = 1279^{+188}_{-145}$ pc) was obtained through the average parallax of the cluster members in [Cantat-Gaudin et al. \(2018\)](#). For this particular object, we replaced its age from N2016 by the averaged *Gaia* determinations and assumed the corresponding dispersion as its uncertainty: $\log[t(\text{yr})] = 9.14 \pm 0.06$.

This paper has been typeset from a \LaTeX file prepared by the author.

Table A2. Morphological age indices and their uncertainties calculated for our OC sample.

O_c	ΔG	$\sigma_{\Delta G}$	ΔBR	$\sigma_{\Delta BR}$	ΔK	$\sigma_{\Delta K}$	ΔJK	$\sigma_{\Delta JK}$
NGC 188	3.21	0.15	0.53	0.02	4.55	0.24	0.44	0.05
NGC 752	1.91	0.27	0.65	0.01	2.76	0.24	0.42	0.03
NGC 1245	0.87	0.26	0.76	0.01	2.01	0.2	0.46	0.04
NGC 1817	1.13	0.15	0.81	0.01	2.85	0.52	0.48	0.03
NGC 2099	0.99	0.30	1.03	0.01	3.36	0.21	0.58	0.04
Trumpler 5	2.88	0.14	0.68	0.01	-	-	-	-
Collinder 110	2.12	0.23	0.71	0.02	3.44	0.27	0.48	0.04
NGC 2354	1.95	0.16	0.68	0.03	3.11	0.23	0.46	0.06
NGC 2355	1.33	0.23	0.82	0.03	2.81	0.45	0.48	0.05
NGC 2360	1.38	0.40	0.77	0.01	2.87	0.25	0.49	0.04
NGC 2423	1.00	0.23	0.76	0.01	2.53	0.29	0.46	0.02
NGC 2420	2.42	0.05	0.60	0.01	3.49	0.08	0.41	0.03
NGC 2447	0.96	0.27	1.01	0.02	2.42	0.22	0.55	0.06
NGC 2477	0.70	0.13	0.85	0.01	2.37	0.05	0.55	0.05
NGC 2527	0.65	0.13	0.90	0.01	2.54	0.49	0.56	0.02
NGC 2539	0.96	0.22	0.97	0.02	2.51	0.37	0.54	0.02
NGC 2660	1.03	0.19	0.70	0.02	2.85	0.25	0.51	0.05
NGC 2682	3.05	0.2	0.55	0.03	4.12	0.22	0.39	0.05
IC 2714	1.60	0.36	1.07	0.02	3.85	0.23	0.65	0.04
NGC 3960	0.86	0.41	0.84	0.03	2.77	0.38	0.53	0.04
NGC 4337	1.51	0.22	0.61	0.02	2.60	0.15	0.48	0.04
NGC 4349	1.53	0.34	1.10	0.02	4.23	0.30	0.68	0.05
Collinder 261	3.19	0.17	0.54	0.02	-	-	-	-
NGC 5822	0.57	0.38	0.83	0.02	2.48	0.43	0.49	0.04
NGC 6134	1.49	0.16	0.66	0.01	2.83	0.07	0.48	0.03
NGC 6253	2.82	0.17	0.53	0.01	4.05	0.23	0.48	0.03
IC 4651	2.11	0.19	0.62	0.01	3.62	0.16	0.45	0.05
NGC 6583	1.31	0.26	0.82	0.02	2.78	0.38	0.55	0.07
IC 4756	0.59	0.31	0.84	0.02	2.77	0.31	0.49	0.03
NGC 6705	1.56	0.41	1.22	0.02	4.4	0.49	0.73	0.04
Ruprecht 147	2.81	0.24	0.56	0.02	3.94	0.29	0.46	0.05
NGC 6811	0.90	0.26	0.80	0.01	2.51	0.15	0.49	0.02
NGC 6819	2.59	0.13	0.62	0.01	-	-	-	-
NGC 7789	2.13	0.20	0.70	0.02	3.23	0.24	0.45	0.04

Table A3. Astrophysical parameters of the NGC2354 cluster from the literature: Liu & Pang (2019, LP2019), Cantat-Gaudin et al. (2018, CG2018), Loktin & Popova (2017, L2017), Kharchenko et al. (2005, K2005), Dürbeck (1960, Du1960), Battinelli et al. (1994, Ba1994).

$d(pc)$	$\log[t](yr)$	$E(B - V)$	ref
1850	8.84	0.14	Du1960
1837	8.26	0.14	Ba1994
4085	8.13	0.31	webda
3794	8.10	0.29	K2005
2865.0	8.61	0.666	K2013
3732 ± 1100	$8, 174 \pm 0.242$	0.286 ± 0.057	L2017
1279^{+188}_{-145}	-	-	CG2018
1132	9.07 ± 0.02	0.26	LP2019
1370.0	9.15	0.11	CG2020
1258 ± 42	9.21 ± 0.03	0.17 ± 0.02	D2021

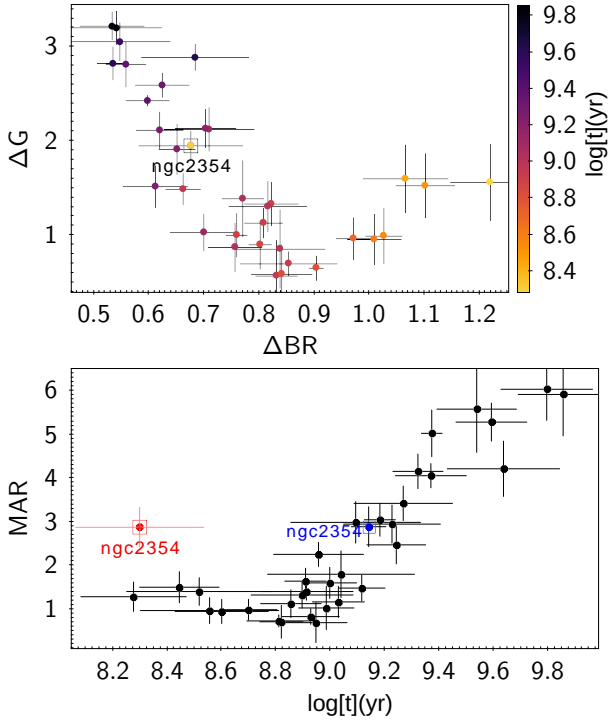


Figure A2. Top: Relation ΔBR versus ΔG . NGC 2354 highlight by a black square. The colour bar represents the age values. Bottom: Relation $\log[t]$ versus MAR. NGC 2354 is plotted with two different age values and represented by two different colours: red (age value from N2016) and blue (age from average *Gaia* values).